Molecular insight into aqueous-phase photolysis and photooxidation of water-soluble organic matter emitted from biomass burning and coal combustion

Tao Cao[1], Cuncun Xu[1,2], Hao Chen[1,2], Jianzhong Song[1,3,*], Jun Li[1,3], Haiyan Song[4], Bin Jiang[1,3], Yin Zhong[1,3], Ping'an Peng[1,2,3]

[1]State Key Laboratory of Advanced Environmental Technology and Guangdong Provincial Key Laboratory of Environmental Protection and Resources Utilization, Guangzhou Institute of Geochemistry, Chinese Academy of Sciences, Guangzhou 510640, China

[2]University of Chinese Academy of Sciences, Beijing 100049, China

[3]Guangdong-Hong Kong-Macao Joint Laboratory for Environmental Pollution and Control, Guangzhou 510640, China

[4]School of Chemistry, South China Normal University, Universities Town, Guangzhou 510006, China

[*]*Correspondence to:* Jianzhong Song, E-mail: songjzh@gig.ac.cn.

Abstract

Biomass and coal combustion represent substantial contributors to atmospheric water-soluble organic matter (WSOM). It experienced intense photochemical oxidation once entered atmospheric environment, but the resulting changes in WSOM are largely unclear. This study examines the changes in the optical properties, fluorophores, and molecular composition of WSOM derived from the combustion of biomass (specifically rice straw, RS) and coal (from Yulin, YL) during aqueous photolysis and hydroxyl radical (·OH) photooxidation. The results indicate that photochemical aging induces distinct changes in the light-absorbing properties of RS and YL WSOM, characterized by pronounced photobleaching in RS WSOM and photoenhancement in YL WSOM. Additionally, more pronounced alterations were observed during ·OH photooxidation than direct photolysis, for both RS and YL WSOM. Furthermore, a greater proportion of molecules in both RS (61.6%) and YL (65.0%) WSOM were degraded during ·OH photooxidation compared to photolysis (14.9% and 23.1%, respectively), resulting in products with larger molecular weight and higher oxidation levels, including tannin-like substances and newly formed black carbon-like compounds, whereas the products of photolysis were characterized by relative minor alteration. These findings provide new insights into the photochemical evolution of combustion-derived WSOM and help to predict its effects in environmental and climate changes.

1. Introduction

Water-soluble organic matter (WSOM) consists of diverse array of polar organic species, which is ubiquitous in atmospheric aerosols, cloud, fog, and rain waters (Sun et al., 2023; Wang et al., 2019). WSOM can not only alter the hygroscopicity and surface tension of aerosol, influence the formation of cloud condensation nuclei, but also has significant effects on the radiative forcing of aerosols, thereby playing crucial roles in atmospheric environment and climate change (Sun et al., 2011; Chen et al., 2019; Lee et al., 2022). Due to its high reactivity, WSOM also contributes to atmospheric chemistry and the formation of organic aerosols. Moreover, WSOM has the potential to catalyze the generation of reactive oxygen species, posing adverse impacts on human health (Bhattu et al., 2024; Bates et al., 2019).

Multiple sources of WSOM have been identified, including primary emissions from biomass burning (BB), coal combustion (CC), vehicular emissions, and secondary formation through the photochemical transformation of volatile organic compounds (Tang et al., 2020; Jiang et al., 2023; Cao et al., 2023). Among these sources, BB has been recognized as a significant contributor to atmospheric WSOM in numerous regions, including East Asia, Southeastern Asia (Liu et al., 2021; Zheng et al., 2017), the Amazon rainforest (Malavelle et al., 2019), and North America (Gallo et al., 2023; Ceamanos et al., 2023). Furthermore, domestic coal combustion also serves as a crucial primary source of atmospheric WSOM in northern China and India (Bikkina et al., 2020; Liu et al., 2022), as well as in Poland (Casotto et al., 2023). It is important to note that the combustion-derived primary WSOM experiences considerable aging upon entering

the atmosphere (Sumlin et al., 2017; Schnitzler et al., 2022). For instance, studies have reported a marked decrease in the light absorption of water-soluble brown carbon (BrC) during transport over distances exceeding 6000 km from the Indo-Gangetic Plain to the Himalayan region (Dasari et al., 2019; Choudhary et al., 2022). Additionally, observations of wildfire plumes in North America have demonstrated a reduction in the mass absorption coefficient as the plume ages (Bali et al., 2024). Nonetheless, the concentrations, light absorption properties, and chemical characteristics of WSOM undergo significant alterations throughout the atmospheric aging process.

Field and laboratory studies demonstrated that aqueous photochemical processes including direct photolysis and secondary photochemistry involving with oxidants (e.g., hydroxyl radical (·OH), O_3), are ubiquitous and play a significant role in the transformation of atmospheric WSOM (Hems et al., 2021; Manfrin et al., 2019). Research conducted by Cai et al. (2020) revealed that the aqueous photochemistry of BB WSOM can produce highly oxygenated compounds, which subsequently enhance the oxidation state of WSOM in atmospheric samples. Furthermore, the ·OH photooxidation of BB-derived organic species (e.g., 4-methylsyringol, eugenol) has been found to form light-absorbing products, indicating a potential pathway for secondary organic aerosol (SOA) (Liu et al., 2022; Li et al., 2023; Arciva et al., 2022). Additionally, the ·OH photooxidation of freshly emitted BB WSOM initially result in an increase in its absorption capacity, which is later followed by a photobleaching process during the photoaging (Hems et al., 2021; Wong et al., 2017). These finding underscore the dynamic nature of WSOM due to the photolytic aging, however, further

insights into the molecular transformations leading to these observations remain unclear. Moreover, while the chemical composition of WSOM emitted from BB and CC differs, it remains unclear whether distinct classes of molecules exhibit varying behaviors during photochemical processes.

To address these inquires, the photochemical aging of WSOM emitted from both biomass burning and coal combustion was systematically investigated through direct photolysis and OH photooxidation in the aqueous phase. The objectives are (1) to compare the optical evolution of BB and CC WSOM under the photolysis and ·OH photooxidation; and (2) to elucidate photochemical transformation of BB and CC WSOM at a molecular level by using fourier transform ion cyclotron resonance mass spectrometry (FT-ICR MS). The information obtained will enhance understanding of the atmospheric oxidation processes of combustion-derived WSOM and their subsequent environmental and climatic effects.

2. Materials and methods

2.1. Preparation of WSOM samples

Rice straw (RS) and Yulin coal (YL) were selected as representative biomass and coal fuel materials for the preparation of combustion-derived WSOM samples. The detailed information of RS and YL were provided in Text S1 and Table S1 in the supporting information (SI). These materials are commonly utilized for heating and cooking in rural households, particularly during winter season in northern China. Additionally, RS residue is also burned in agriculture field (Zhang et al., 2023; Huang

et al., 2022). The smoke samples emitted from combustion process were collected in a laboratory-controlled combustion system in our laboratory and more detailed information can be seen in our previous studies (Cao et al., 2021; Li et al., 2018). Immediately after collection, the filters were wrapped with baked aluminum foil and stored in a refrigerator (−20 ºC).

Prior to conducting photolysis and photooxidation experiments, the WSOM fraction was extracted using ultrapure-water. Briefly, filter sample was cut into pieces and placed in 100 mL glass bottle, to which 60 mL ultrapure water was added. After ultrasonically extracted for 30 min, the extract was filtered through a 0.22 μm polytetrafluoroethylene syringe filter (Anpel, ANPEL Laboratory Technology (Shanghai) Inc.). The organic carbon concentration of WSOM solution was measured by a total organic carbon analyzer (VCPH analyzer, Shimadzu, Kyoto, Japan) following the non-purgeable organic carbon protocol. After the removal of inorganic carbon, the sample was oxidized at high temperature (680 °C) to generate CO_2 and then determined by non-dispersive infrared detector. Before photochemical reaction, WSOM solution was diluted to 20 mgC/L by ultrapure water (Gu et al., 2024; Zhang et al., 2022). The detailed information can be found in Text S2 of SI.

2.2. Photolysis and ·OH photooxidation experiment

The photolysis and ·OH photooxidation experiments were conducted in a photoreactor with three replicates, where quartz cell containing WSOM solution were continuously exposed to radiation. Briefly, 100 mL of 20 mgC/L WSOM solution was magnetically stirred in a 250 mL cylindrical quartz cell equipped with water circulating

jacket to maintain a constant temperature of 25 ºC. For the photolysis experiment, the WSOM solution was irradiated from the top by Xenon lamp (PL-XQ500W, Beijing Princess Technology co. ltd) with an output energy of 500W at 0.2 m. The irradiation energy at the water surface is 12.5 mW/cm^2 (290−400 nm), which is about 5.2 times higher than the light intensity of actual solar exposure (Figure S1, obtained at noon of May 20, 2023, Guangzhou) and the actinic flux of Xe lamp is 5.4×10^{-5} Einstein/cm^2/s^1 as determined by the p-nitroanisole/pyridine actinometer method (Laszakovits et al., 2016). For the ·OH photooxidation experiments, 3mM H_2O_2 was added to the WSOM solution as a photolytic source of ·OH radicals upon irradiation (Zhao et al., 2015; Fan et al., 2023; Arciva et al., 2024). Based on the conditional experiment, it was found that approximately 35.6%±4.6% of H_2O_2 was consumed after a 24-hour reaction period. This indicates that there was a sufficient amount of ·OH present to react with WSOM during the ·OH photooxidation experiment. For each experiment, 4 mL samples were withdrawn periodically (0, 1, 2, 4, 8, 12, 24h) from the reactor and then diluted to 20 mL for further analysis. The photolysis and ·OH photooxidation experiment were both carry out the dark control synchronously follow the conditions as introduced above. The results showed that no significant changes were observed for the organic carbon content and the UV-vis absorption of WSOM within the reaction time.

2.3. Spectroscopy measurement

The UV-vis absorption of WSOM was measured using a UV-vis spectrophotometer (UV-2600i, Shimadzu, Japan) within the wavelength range of 200 – 700 nm. Excitation-emission matrix (EEM) spectra were recorded by three-dimensional

fluorescence spectrophotometer (Aqualog, HORIBA Scientific, USA). The scanning ranges for excitation (Ex) and emission (Em) were 240–800 nm and 250-800 nm, respectively. Ultrapure water (18.2MΩcm^{-1}) was used as blank reference and correcting the fluorescence intensity unit by the Raman peak area of water (R.U.). In addition, the corresponding absorption spectra were used to correct the EEM for inner-filter effects (IFEs) according to the previous studies if the absorbance was higher than 0.05 at 250 nm (Tang et al., 2020; He and Hur, 2015; Murphy et al., 2013). The PARAFAC modeling procedure was conducted in MATLAB 2021b (Mathwork.Inc, USA) by the drEEM toolkit (Murphy et al., 2018; Pucher et al., 2019). More information and data processing details are provided in Text S3 of SI.

2.4. High-resolution mass spectrometry analysis

The molecular characteristics of WSOM before and after photolysis and ·OH photooxidation were measured with a solariX XR FT-ICR MS (Bruker Daltonik GmbH, Bremen, Germany) equipped with a 9.4T refrigerated actively shielded superconducting magnet and a Paracell analyzer cell. The WSOM samples used for FT-ICR MS analysis were desalted by solid phase extraction cartridge (Oasis HLB, 200 mg, Waters, Milford, MA, USA) as introduced in our previous studies (Song et al., 2019; Song et al., 2018; Song et al., 2022). The detailed measurement condition and the calculation of corresponding indexes (e.g. double bond equivalents (DBE) and modified aromaticity index (AI_{mod})) are described in Text S4 in SI. For better elucidate the transformation of RS and YL WSOM, the photochemical resistant, degraded, and produced molecules were investigated (Fan et al., 2024; Gu et al., 2024).

3. Results and discussion

3.1. Effect of photolysis and ·OH photooxidation on the light absorption of WSOM

The absorption spectra of RS and YL WSOM during photolysis and ·OH photooxidation are illustrated in Figure 1a-d. It can be observed that the absorbance of RS WSOM gradually decrease as aging time increasing during both photolysis and ·OH photooxidation, indicating substantial photobleaching (Fan et al., 2024; Zhao et al., 2022). Moreover, the reduction in absorbance during ·OH photooxidation is more obvious than that in photolysis, indicated that RS WSOM undergoes greater degradation during ·OH photooxidation. In contrast, the absorbance of YL WSOM present different variation during the photolysis and ·OH photooxidation. Specifically, the absorbance in the short wavelength range of 210-240 nm decreases gradually with aging time, while the absorbances at wavelengths exceeding 360 nm increase. This phenomenon is characteristic of photoenhancement, which aligns with finding reported in previous studies concerning nitrate-mediated photooxidation of guaiacol and 5-nitroguaiacol as well as photooxidation of mixed aromatic carbonyls (Go et al., 2024; Yang et al., 2021).

To quantitatively assess the changes in light-absorbing substances during photolysis and ·OH photooxidation, the absorption coefficients at 254 nm (α_{254}) and 365 nm (α_{365}) were calculated (Fan et al., 2024; Zou et al., 2023). As shown in Figure 1e, the α_{254} values for both RS and YL WSOM consistently decline during photolysis and ·OH photooxidation, with a more significant reduction observed during ·OH photooxidation. These results are consistent with earlier studies on dark ·OH oxidation

of BB WSOM, indicating that the presence of ·OH radicals accelerate the degradation of aromatic structures within WSOM (Fan et al., 2024; Ye et al., 2020). Additionally, the reduction of α_{254} values was always greater for RS WSOM than for YL WSOM, suggesting that RS WSOM are more susceptible to photochemical degradation.

The α_{365} values for RS and YL WSOM exhibit different variations under photolysis and ·OH photooxidation. As illustrated in Figure 1f, the α_{365} value for RS WSOM gradually decrease with prolonged photolysis, while it initially increased slightly before decreasing during ·OH photooxidation. Similar observation has been made in the photochemical aging of wood smoke BrC and monomeric phenolic compounds, suggesting the formation of new compounds with significant light-absorbing capacity during the initial stage of ·OH photochemical reaction (Hems et al., 2021; Wong et al., 2017; Lee et al., 2014). In contrast, the α_{365} values of YL WSOM presented markedly different trends, increasing during 24h photolysis and initially rising for 12h before decreasing from 12h to 24h during ·OH photooxidation. These results indicates that the products generated from photochemical reaction of YL WSOM possess enhanced light absorbance in the near-UV and visible regions, which are also observed in the aqueous phase oxidation of aromatic compounds such as phenols (Arciva et al., 2024; Smith et al., 2016). The proposed mechanism may involve the aromatization of phenolic compounds and ·OH-functionalization of aromatic compounds, leading to the formation of the strong light-absorbing substances at longer wavelength (Li et al., 2023).

3.2. EEM-PARAFAC of WSOM during the photolysis and ·OH photooxidation

The EEM-PARAFAC model has successfully identified three distinct fluorescent

components (C1–C3) within RS and YL WSOM. As shown in Figure 2a, C1 displays excitation/emission peaks at Ex/Em = 270/325 nm, which are attributed to protein-like substances, including tyrosine-like substances (Podgorski et al., 2018; Hu et al., 2023), as well as non-nitrogenous containing species such as phenol-like compounds (Cao et al., 2023). C2 (240, 320/420 nm) and C3 (240/350 nm) both assigned to humic-like substances (Hu et al., 2023; He et al., 2023; Fan et al., 2021). Due to the fluorescence distributed at longer wavelengths are mainly associated of larger molecular weight and highly oxygenated of fluorophores (Cao et al., 2023), thereby suggesting that the longer emission wavelengths of C2 might be associated with highly oxygenated humic-like fluorophores with higher molecular weight and aromaticity, while C3 could be more relevant to less oxygenated structures and conjugated systems. Furthermore, fluorophores contain same position with C2 have been observed during the photooxidation of vanillic acid and ozone oxidation of BB BrC (Fan et al., 2021; Tang et al., 2020), indicating C2 may be closely related with the products formed through atmospheric oxidation processes.

To quantitatively access the changes in the distribution of fluorophores during the photochemical process, total fluorescence intensity (TFI) was calculated. As depicted in Figure 2d, the TFI values for RS and YL WSOM showed a comparable decline during both photolysis and ·OH photooxidation, with a pronounced reduction during ·OH photooxidation. These results indicate that fluorophores are more susceptible to degradation or quenching by ·OH attacks than by direct photolysis in both BB and CC WSOM. On the one hand, more aromatic structures in WSOM may be disrupted by

·OH radical, resulting a more significant reduction in fluorophores. On the other hand, the ·OH photooxidation also lead to an increase in carboxyl groups, which are the typical electron-withdrawing groups. thereby contributing to a reduction or quenching of fluorescence in WSOM.

Moreover, the relative contribution of the three fluorophores in RS and YL WSOM varied throughout photochemical processes, with more significant changes noted during ·OH photooxidation (Figure 2e-h). It is obvious that the increases in C2 are 49% and 56% for RS and YL WSOM during ·OH photooxidation, which is significantly higher than that 5% and 14% during photolysis. These can be explained by the formation of more highly oxygenated humic-like fluorophores due to ·OH photooxidation (Zhang et al., 2022; Fan et al., 2024). In contrast, fluorophore C3 greatly declined by 35% and 56% for RS and YL WSOM, respectively, during ·OH photooxidation. Previous studies have linked fluorophore C3 to less-oxygenated fluorescent substances resulting from primary combustion (Cao et al., 2023; Chen et al., 2016), which can be oxidated and gradually removed during the ·OH photooxidation process. Comparatively, the contributions of three fluorescent components in RS and YL WSOM both display relatively minor variations under photolysis, suggesting the lower selectivity of photolysis. These notable variations in both the subgroup and intensity of fluorophores suggest their potential utility as indicator of the atmospheric oxidation processes experienced by fresh emissions (Fan et al., 2024; Ye et al., 2025).

3.3. Changes in molecular characteristics of RS and YL WSOM

Figure 3 showed the FT-ICR MS spectra of RS and YL WSOM before and after

undergoing photochemical oxidation. A total of 5114 to 6383 molecules were identified within the m/z range of 100-600, with a predominant concentration of peaks observed between 150 to 400. These finding are indicative of the molecular characteristics typical of organic compounds resulting from BB and coal combustion emissions (Tang et al., 2020; Song et al., 2018; Song et al., 2022). The identified formulae were categorized based on their elemental compositions into four groups: CHO, CHON, CHOS, and CHONS (Tang et al., 2020; Song et al., 2018). As shown in Figure 3, CHO and CHON compounds are the dominant compounds (95.8%-98.4%) in RS WSOM, with minor fluctuations following photolysis and ·OH photooxidation. Similar changes were also observed for BB WSOM under dark ·OH oxidation (Fan et al., 2024). In contrast to RS WSOM, YL WSOM contain not only high content of CHO (47.6%) and CHON (33.1%), but also significant S-containing substances (CHOS and CHONS, 19.2%). Figure 3 reveals notable differences in the composition of compound groups within YL WSOM. The CHO compounds in fresh YL WSOM are 47.6%, which increased to 76.1% and 84.2% after photolysis and ·OH photooxidation, respectively. Whereas, the CHON compounds decreased from 33.1% to 13.4% and 13.6%, respectively. Additionally, S-containing compounds demonstrated a marked decrease following photolysis and ·OH photooxidation for YL WSOM. These discrepancies may be attributed to the inherent differences in molecular composition between RS WSOM and YL WSOM, which exhibit varying sensitivities to photolysis and ·OH photooxidation.

3.3.1. Molecular properties

The intensity weighted average values of various molecular parameters, including

molecular weight (MW_w), elemental ratios, double bond equivalents (DBE_w), modified aromaticity index ($AI_{mod,w}$), and nominal oxidation state of carbon ($NOSC_w$) of RS and YL WSOM before and after photochemical aging were summarized in Table S2. It is evident that the molecular characteristics of WSOM underwent significant alterations following photolysis and ·OH photooxidation. Specifically, the MW_w value of fresh RS WSOM is 252, which increased to 288 and 319 after photolysis and ·OH photooxidation, respectively. The similar trend was observed for YL WSOM, where the MW_w values increased from 231 to 268 and 303, respectively. These observations in molecular weight aligned with findings related to the aqueous-phase photochemical oxidation of wood smoke WSOM, but no significant change in molecular weight was observed in the aqueous-phase dark ·OH oxidation of BB WSOM (Fan et al., 2024; Wong et al., 2019). Such changes may be attributed to the newly formation of higher MW molecules through the oligomerization reactions and the resistance of high MW ones during photochemical aging (Gu et al., 2024; Fan et al., 2024; Go et al., 2024; Waggoner et al., 2015; Carena et al., 2023). Furthermore, it is noteworthy that the MW_w values for both RS and YL WSOM following ·OH photooxidation were greater than that after photolysis, suggesting that ·OH photooxidation exerts a more pronounced aging effect.

As detailed in Table S2, the $AI_{mod,\ w}$ value of fresh RS WSOM is 0.44, which subsequently decreased to 0.42 and 0.36 after photolysis and ·OH photooxidation, respectively. Similar variation was noted for YL WSOM, where the $AI_{mod,\ w}$ value decreased from 0.56 to 0.52 and 0.47, respectively. Moreover, the reduction in $AI_{mod,w}$ values were more pronounced for both RS and YL WSOM subjected to ·OH

304 photooxidation. This significant decreasing in $AI_{mod,w}$ values of BB WSOM was also
305 observed during the dark ·OH oxidation (Fan et al., 2024). These results indicate that
306 the aromatic structures within WSOM were disrupted during photochemical processes,
307 while ·OH photooxidation resulting in more significant breakdown (Zhao et al., 2022).
308 The O/C_w and $NOSC_w$ values were used to estimate the oxidation degree of the
309 formulae in WSOM. As shown in Table S2, the O/C_w of RS WSOM increased from
310 0.38 to 0.43 and 0.59 after photolysis and ·OH photooxidation, respectively, indicating
311 an increase in the number of O atom within the molecular post-oxidation. Notably, the
312 $NOSC_w$ values exhibited a similar trend to that of O/C_w. These observations are
313 consistent with findings related to BB WSOM under dark ·OH oxidation and the
314 photochemical transformation of DOM (Gu et al., 2024; Zhang et al., 2022; Fan et al.,
315 2024), suggesting a substantial incorporation of O-containing functional groups into
316 carbon structures during the photolysis and ·OH oxidation. The O/C_w and $NOSC_w$
317 values for YL WSOM demonstrated analogous changes following ·OH photooxidation,
318 increasing from 0.46 to 0.57 and from 0.06 to 0.14, respectively. However, the O/C_w
319 and $NOSC_w$ values for YL WSOM exhibit slight decrease after photolysis, declining
320 from 0.46 to 0.43 and from 0.06 to -0.09, respectively. These findings indicate that the
321 photochemical evolution of WSOM is significantly influenced by their molecular
322 composition. Nonetheless, it is undoubtedly that the O/C_w and $NOSC_w$ values of aged
323 WSOM resulting from ·OH photooxidation are significantly higher than those resulting
324 from photolysis, indicating a more robust oxidation process.
325 To further elucidate the molecular distribution of WSOM, van Krevelen (VK)

diagrams were constructed by plotting the H/C ratio versus O/C ratio. As indicated in Figure S2, the identified compounds were classified into seven distinct regions (Sun et al., 2023; Song et al., 2018): (I) lipids-like, (II) protein/animo sugars, (III) carbohydrates-like, (IV) unsaturated hydrocarbons, (V) lignin/CRAMs-like, (VI) condensed aromatic, and (VII) tannins. It is obvious that lignin/CRAMs-like compounds emerged as the predominant constituents, comprising 83.1% and 88.4% of the fresh RS and YL WSOM (Table S3), respectively. The proportion of these compounds remained stable following photolysis; however, a decline was observed following ·OH photooxidation, with the contents decreasing from 83.1% to 63.3% for RS WSOM and from 88.4% to 73.9% for YL WSOM. Lipid compounds were also identified in both fresh RS and YL WSOM, with relative higher contents in RS WSOM, however, a significant reduction in lipid content was noted after ·OH photooxidation for both RS WSOM and YL WSOM. This trend aligns with observations of DOM under UV irradiation, where lignin and lipids were identified as the most active component involved in molecular conversion (Gu et al., 2024). Conversely, the content of tannins-like substances in both RS and YL WSOM greatly increased due to ·OH photooxidation. This suggest that the attack by ·OH radical lead to the formation of more polar tannins compounds, indicating the potential contribution of multiple oxygen-enrich groups (i.e., carboxyl) to the aged WSOM. Such additional functional groups may enhance the polarity and reactivity of WSOM, thereby influencing their optical properties, chemical reactivity, and interactions with other atmospheric components. It is noteworthy that more condensed aromatic compounds were observed in aged WSOM subjected to

photochemical process, especially ·OH photooxidation (e.g., the left and bottom of VK diagrams, Figure S2). Furthermore, as shown in Table S3, the content of condensed aromatic compounds increased from 1.08% to 1.55% and 4.86% (RS WSOM) and 2.86% to 4.08% and 5.38% (YL WSOM) after photolysis and ·OH photooxidation, respectively. These findings strongly support the notion that condensed aromatic molecules are formed through the photochemical reactions, particularly the ·OH photooxidation reaction.

3.3.2. Comparison of the transformation of WSOM induced by photolysis and ·OH photooxidation

To enhance the understanding of molecular transformations occurring in RS and YL WSOM, the photochemical resistant, degraded, and produced molecules were investigated. The formulae identified both before and after photochemical aging were assigned to resistant; unique formulae before reaction represented the degraded molecules; whereas unique formulae after reaction were considered to newly produced molecules (Figure 4) (Gu et al., 2024; Fan et al., 2024; Zhao et al., 2022). It is important to acknowledge that the molecules categorized as resistant may also include those generated from the photochemical reaction, but with the formulae to those in fresh molecules. As presented in Table S4, approximately 14.9% of the total number of formulas in fresh RS WSOM and 23.1% in YL WSOM were degraded through photolysis, resulting in the formation of 26.0% (RS WSOM) and 31.7 % (YL WSOM) of newly produced formulae in the aged WSOM, respectively. In contrast, much higher content of formulae (61.6% of RS WSOM and 65.0% of YL WSOM) were degraded

by ·OH photooxidation and led to higher content (57.0%-61.0%) of new formulae. These findings suggest that ·OH photooxidation possesses greater oxidative potential, resulting in a more substantial degradation and transformation of molecules.

As shown in Figure 4b, 4e, 4h and 4k, the majorities of the degraded molecules were found in regions characterized by in O/C (<0.6) within VK diagram. In contrast, the newly produced molecules were concentrated in the regions of $0.3 < O/C < 0.9$. This finding implies that molecules with low O/C underwent oxidation during photolysis and ·OH photooxidation processes, resulting in their transformation into oxygen-enriched structures, especially through ·OH photooxidation. Furthermore, notable differences were observed in the VK diagrams corresponding to photolysis and ·OH photooxidation. It is obvious that the degraded molecules from RS and YL WSOM were distributed in the same region of the VK diagrams; however, the newly formed molecules resulting from distinct photochemical reactions were distributed across different regions (Figure S3). For example, the molecules produced from the photolysis of RS WSOM primarily located in the range of $0.3 < O/C < 0.7$ and $0.5 < H/C < 1.7$, whereas those generated through ·OH photooxidation were found in two separate regions. The majorities of these molecules were concentrated in the range $0.4 < O/C < 0.9$ and $0.4 < H/C < 2.0$, indicating a higher formation of oxygenated compounds through ·OH photooxidation. As illustrated in Figure 4f and 4l, the presence of tannin-like compounds in the molecules produced after ·OH photooxidation were much higher than that formed after photolysis for both RS and YL WSOM. These results indicate that the ·OH photooxidation process substantially enhanced the abundance of O-

containing functional groups within the molecules, as well as the overall oxidation state of WSOM. Additionally, certain condensed aromatic molecules were identified in the regions VI in Figure 4f and 4l and S2, showing the newly production of condensed aromatics during ·OH photooxidation. According to Table S5, these newly formed condensed molecules were identified in both RS and YL WSOM, accounting for 11.6% and 4.7% of the total produced molecules (intensity weighted). These compounds exhibited lower H/C_w (0.55 and 0.60) and O/C_w (0.14 and 0.17) ratios alongside higher $AI_{mod,w}$ (0.76 and 0.77) values, indicating a predominance of highly aromatic structures. Moreover, they consisted with CHO, CHON, CHOS, and CHONS, among which CHON is the highest components (57.7% and 58.0%) for both RS and YL WSOM. It is noteworthy the O/N_w ratios for CHON and the O/S_w ratios for CHOS were relatively low, suggesting that the N-containing and S-containing functional group here may mainly comprised with reduced groups. According to previous studies, the condensed aromatic compounds are usually assigned to traditional dissolved black carbon (BC) molecules derived from combustion (Fan et al., 2023; Liu et al., 2022; Yan et al., 2022). These compounds share similar molecular characteristics, such as lower H/C_w ratios and higher $AI_{mod,w}$ values. However, our study suggesting that ·OH photochemical oxidation may also contribute to the formation of BC-like molecules. In contrast, the ·OH oxidation that without the presence of light, initiated by Fenton chemistry, does not produce these BC-like substances (Fan et al., 2024). This possibly indicates that the formation of highly aromatic BC-like molecules requires both ·OH oxidation and photoreactions to occur.

As shown in Table S6, the degraded molecules exhibited lower $AI_{mod,w}$ values and O/C_w ratio, and higher MW_w, DBE_w, and H/C_w values compared to the resistant molecules. For example, the $AI_{mod,w}$ value and O/C_w ratio of the degraded molecules of RS WSOM are 0.33 and 0.33, respectively, which are lower than the corresponding values of 0.38 and 0.45 for the resistant molecules during photolysis. Conversely, the MW_w, DBE_w, and H/C_w ratio for the degraded molecules are 392, 8.3, and 1.29, significantly higher than that for the resistant molecules. Similar differences were noted between the resistant and degraded molecules in RS WSOM subjected to ·OH photooxidation, as well as in YL WSOM underwent both photolysis and ·OH photooxidation. These differences indicate that the WSOM susceptible to photochemical aging are those molecules with higher molecular weight, double bond intensity, and aliphatic structures but with lower aromaticity and O-containing group.

In comparison, the newly formed molecules within RS and YL WSOM demonstrate elevated O/C_w, DBE_w, and MW_w values. For example, the newly formed molecules for RS WSOM resulting from photolysis possess higher O/C_w (0.48), DBE_w (12.0), and MW_w (473) than the degraded molecules. These results indicate that photolysis generates a greater quantity of high molecular weight compounds, which also contain more oxygenated functional groups, such carbonyl. Furthermore, the differences between the degraded and resistant molecules during ·OH photooxidation are pronounced than that during the photolysis process, suggesting that a more extensive aging reaction occurs during ·OH photooxidation. However, the variation in $AI_{mod,w}$ value between the degraded and produced molecules differ across samples. In

the case of RS WSOM, the produced molecules exhibit higher $AI_{mod,w}$ values than the degraded molecules during photolysis process, yet they are very similar during ·OH photooxidation. Additionally, distinct changes in $AI_{mod,w}$ values were observed for YL WSOM during photolysis, where the $AI_{mod,w}$ value of newly produced molecules is lower than that of degraded molecules, and the proportion of aromatic and condensed aromatic compounds decreased for YL WSOM after photolysis. These discrepancies may be due to the produced molecules defined represent only a subset of those generated during the aging process.

3.4. Comparison of the photochemical evolution of WSOM from biomass burning and coal combustion

The photochemical evolution of WSOM originating from BB and CC were comparably investigated in our study. Our results indicate that the absorption spectra of RS and YL WSOM exhibit a decreasing trend at ranges below 240 nm during photolysis and ·OH photooxidation. However, notable differences were observed between the two types of WSOM. For example, the α_{365} value for RS WSOM consistently decreased throughout the photolysis and ·OH photooxidation, whereas YL WSOM displayed a progressive increase in this value. These differences may be attributed to the inherent differences in WSOM derived from biomass burning compared to that from coal combustion (Cao et al., 2021; Song et al., 2018). The results indicate that WSOM derived from various sources may undergo distinct changes in absorbance during photochemical aging, potentially leading to varying impacts on climate change and radiation balance.

458 Furthermore, the TFI values for both RS and YL WSOM exhibit a gradual decline
459 during photolysis and ·OH photooxidation with no significant differences between the
460 two. However, the variations in fluorophore composition within RS and YL WSOM
461 were markedly different. For example, three fluorophores in RS WSOM remained
462 relative stable during photolysis, while the less-oxygenated fluorophores C3 in YL
463 WSOM gradually decreased. These may indicate that the fluorophores C3 in YL
464 WSOM are more susceptible to photolytic degradation. These results suggest that the
465 molecular composition of identical fluorescent component in WSOM derived from
466 different sources may exhibit notable differences.

467 As previously discussed, there are notable similarities in the molecular alterations
468 observed in RS and YL WSOM after photolysis aging. Specifically, the MW_w values
469 for both RS and YL WSOM exhibited an increase after photochemical processes,
470 suggesting the formation of high MW molecules through the oligomerization reaction
471 and the resistance of high MW ones during photochemical aging. Furthermore, the
472 $AI_{mod,w}$ values always decreased, while the O/C ratios consistently increased for the
473 both aged RS and YL WSOM. These results indicate the broken of aromatic structures
474 and the formation of O-containing groups within WSOM as a result of photochemical
475 processes. However, distinct differences in molecular characteristics between RS and
476 YL WSOM were observed, which may influence their respective changes due to
477 photochemical reactions. For example, CHON compound in RS WSOM exhibit minor
478 variation after photochemical reactions, whereas it greatly decreased in YL WSOM.
479 Notably, RS WSOM experienced a greater degradation of lipids during photolysis

and ·OH photooxidation, leading to the production of carbohydrate or tannin-like substances (Table S3).

4. Environmental significance

Biomass and coal combustion releases considerable quantities of WSOM into the atmosphere, which undergo significant photochemical transformations under light irradiation, resulting in considerable uncertainty regarding its physical and chemical characteristics, as well as reactivity in the atmospheric environment. The present study investigated the optical and molecular evolution in WSOM derived from BB and CC (i.e., RS and YL WSOM) during aqueous phase photolysis and ·OH photooxidation. The findings indicate a marked reduction in light absorption of RS WSOM at 365 nm during photochemical processes and more pronounces for the ·OH photooxidation, indicating a stronger photobleaching. In contrast, a notable photoenhancement was observed for YL WSOM during the photochemical processes. These results suggest that the alteration in light absorption of WSOM are closely linked to the chemical composition of fresh WSOM.

At the molecular level, the degradation of aromatic structures within WSOM was evident, accompanied by the formations of O-containing polar groups (e.g., carbonyl, carboxyl groups), as a result of the photochemical reactions, particularly during ·OH photooxidation. These results indicates that the oxidation degree and severity of ·OH photooxidation is much higher than that of photolysis, leading to the variations in the optical properties of WSOM. It is worthing noted that the polymerization occurs in both

photolysis and ·OH photooxidation, especially in ·OH photooxidation, as evidenced by an increase in MW_w and the formation of condensed aromatic compounds. These condensed aromatic compounds exhibit similarities to the chemical and molecular structures of combustion derived BC molecules. Therefore, ·OH photochemical oxidation may a potential formation mechanism of BC-like materials.

It is important to note that this study focused solely on WSOM produced from a specific type of biomass and coal samples in laboratory simulated system, which may nor accurately reflect the complexities of combustion processes in real-world scenarios. Therefore, a more comprehensive investigation into the photochemical aging of WSOM from diverse biomass and coal sources, as well as under various conditions in natural environments, is warranted. Furthermore, it is clear that the photochemical aging processes significantly influences their environmental, climate, and health effects, necessitating further exploration in future research endeavors.

Data availability. The research data can used in this study are available from Jianzhong Song (songjzh@gig.ac.cn).

Author contributions. T. Cao and J. Song designed the research and wrote the paper. T. Cao, C. Xu, H. Chen and H. Song, analyzed the combustion-derived WSOM samples during photochemical process. B. Jiang analyzed the WSOM samples by FT-ICR MS. J. Li, Y. Zhong, and P. Peng commented and revised the paper.

Competing interests. The authors declare that they have no conflict of interest

Acknowledgments. This study was supported by the National Natural Science Foundation of China (42192514), Guangdong Major Project of Basic and Applied Basic Research (2023B0303000007), and the Guangdong Foundation for Program of Science and Technology Research (2023B1212060049).

References

Arciva, S., Ma, L., Mavis, C., Guzman, C., Anastasio, C. Formation and loss of light absorbance by phenolic aqueous SOA by ·OH and an organic triplet excited state. Atmos. Chem. Phys., 24, 4473-4485, https://doi.org/10.5194/acp-24-4473-2024, 2024.

Arciva, S., Niedek, C., Mavis, C., Yoon, M., Sanchez, M. E., Zhang, Q., Anastasio, C. Aqueous ·OH Oxidation of Highly Substituted Phenols as a Source of Secondary Organic Aerosol. Environ. Sci. Technol., 56, 9959-9967, https://doi.org/10.1021/acs.est.2c02225, 2022.

Bali, K., Banerji, S., Campbell, J. R., Bhakta, A. V., Chen, L. W. A., Holmes, C. D., Mao, J. Measurements of brown carbon and its optical properties from boreal forest fires in Alaska summer. Atmos. Environ., 324, 120436, https://doi.org/10.1016/j.atmosenv.2024.120436, 2024.

Bates, J. T., Fang, T., Verma, V., Zeng, L., Weber, R. J., Tolbert, P. E., Abrams, J. Y., Sarnat, S. E., Klein, M., Mulholland, J. A., Russell, A. G. Review of Acellular

546 Assays of Ambient Particulate Matter Oxidative Potential: Methods and
547 Relationships with Composition, Sources, and Health Effects. Environ. Sci.
548 Technol., 53, 4003-4019, https://doi.org/10.1021/acs.est.8b03430, 2019.
549 Bhattu, D., Tripathi, S. N., Bhowmik, H. S., Moschos, V., Lee, C. P., Rauber, M., Salazar,
550 G., Abbaszade, G., Cui, T., Slowik, J. G., Vats,, P., Mishra, S., Lalchandani, V.,
551 Satish, R., Rai, P., Casotto, R., Tobler, A., Kumar, V., Hao, Y., Qi, L., Khare, P.,
552 Manousakas, M., Wang, Q., Han, Y., Tian, J., Darfeuil, S., Minguillon, M., Hueglin,
553 C., Conil, S., Rastogi, N., Srivastava, A., Ganguly, D., Bjelic, S., Canonaco, F.,
554 Schnelle-Kreis, J., Dominutti, P. A., Jaffrezo, J., Szidat, S., Chen, Y., Cao, J.,
555 Baltensperger, U., Uzu, G., Daellenbach, K. R., Haddad, I., Prévôt, A. S. H. Local
556 incomplete combustion emissions define the $PM_{2.5}$ oxidative potential in Northern
557 India. Nat. Commun., 15, 3517, https://doi.org/10.1038/s41467-024-47785-5,
558 2024.
559 Bikkina, P., Sarma, V. V. S. S., Kawamura, K., Bikkina, S., Kunwar, B., Sherin, C. K.
560 Chemical characterization of wintertime aerosols over the Arabian Sea: Impact of
561 marine sources and long-range transport. Atmos. Environ., 239, 117749,
562 https://doi.org/10.1016/j.atmosenv.2020.117749, 2020.
563 Cai, J., Zeng, X., Zhi, G., Gligorovski, S., Sheng, G., Yu, Z., Wang, X., Peng, P.
564 Molecular composition and photochemical evolution of water-soluble organic
565 carbon (WSOC) extracted from field biomass burning aerosols using high-
566 resolution mass spectrometry. Atmos. Chem. Phys., 20, 6115-6128,
567 https://doi.org/10.5194/acp-20-6115-2020, 2020.

568 Cao, T., Li, M., Xu, C., Song, J., Fan, X., Li, J., Jia, W., Peng, P. Technical note:
569 Chemical composition and source identification of fluorescent components in
570 atmospheric water-soluble brown carbon by excitation–emission matrix
571 spectroscopy with parallel factor analysis – potential limitations and applications.
572 Atmos. Chem. Phys., 23, 2613-2625, https://doi.org/10.5194/acp-23-2613-2023,
573 2023.
574 Cao, T., Li, M., Zou, C., Fan, X., Song, J., Jia, W., Yu, C., Yu, Z., Ping, P. Chemical
575 composition, optical properties, and oxidative potential of water- and methanol-
576 soluble organic compounds emitted from the combustion of biomass materials and
577 coal. Atmos. Chem. Phys., 21, 13187-13205, https://doi.org/10.5194/acp-21-
578 13187-2021, 2021.
579 Carena, L., Zoppi, B., Sordello, F., Fabbri, D., Minella, M., Minero, C.
580 Phototransformation of Vanillin in Artificial Snow by Direct Photolysis and
581 Mediated by Nitrite. Environ. Sci. Technol., 57, 8785-8795,
582 https://doi.org/10.1021/acs.est.3c01931, 2023.
583 Casotto, R., Skiba, A., Rauber, M., Strahl, J., Tobler, A., Bhattu, D., Lamkaddam, H.,
584 Manousakas, M. I., Salazar, G., Cui, T., Canonaco. F., Samek. L., Ryś, A., Haddad,
585 I. E., Kasper-Giebl, A., Baltensperger, U., Necki, J., Szidat, S., Styszko, K., Slowik,
586 J. G., Prévôt, A. S.H., Daellenbach. K. R. Organic aerosol sources in Krakow,
587 Poland, before implementation of a solid fuel residential heating ban. Sci. Total.
588 Environ., 855, 158655, https://doi.org/10.1016/j.scitotenv.2022.158655, 2023.
589 Ceamanos, X., Coopman, Q., George, M., Riedi, J., Parrington, M., Clerbaux, C.

Remote sensing and model analysis of biomass burning smoke transported across the Atlantic during the 2020 Western US wildfire season. Sci. Rep., 13, 16014, https://doi.org/10.1038/s41598-023-39312-1, 2023.

Chen, Q., Wang, M., Wang, Y., Zhang, L., Li, Y., Han, Y. Oxidative Potential of Water-Soluble Matter Associated with Chromophoric Substances in $PM_{2.5}$ over Xi'an, China. Environ. Sci. Technol., 53, 8574-8584, https://doi.org/10.1021/acs.est.9b01976, 2019.

Chen, Q., Miyazaki, Y., Kawamura, K., Matsumoto, K., Coburn, S., Volkamer, R., Iwamoto, Y., Kagami, S., Deng, Y., Ogawa, S., Ramasamy, S., Kato, S., Ida, S., Kajii, Y., Mochida, M. Characterization of Chromophoric Water-Soluble Organic Matter in Urban, Forest, and Marine Aerosols by HR-ToF-AMS Analysis and Excitation-Emission Matrix Spectroscopy. Environ. Sci. Technol., 50, 10351-10360, https://doi.org/10.1021/acs.est.6b01643, 2016.

Choudhary, V., Gupta, T., Zhao, R. Evolution of Brown Carbon Aerosols during Atmospheric Long-Range Transport in the South Asian Outflow and Himalayan Cryosphere. ACS Earth. Space. Chem., 6, 2335-2347, https://doi.org/10.1021/acsearthspacechem.2c00047, 2022.

Dasari, S., Andersson, A., Bikkina, S., Holmstrand, H., Budhavant, K., Satheesh, S., Asmi, E., Kesti, J., Backman, J., Salam, A., Bisht, D. S., Tiwari, S., Hameed, Z.,Gustafsson, Ö. Photochemical degradation affects the light absorption of water-soluble brown carbon in the South Asian outflow. Sci. Adv., 5, eaau8066, https://doi.org/10.1126/sciadv.aau8066, 2019.

612 Fan, J., Duan, T., Zou, L., and Sun, J.: Characteristics of dissolved organic matter
613 composition in biochar: Effects of feedstocks and pyrolysis temperatures, Environ.
614 Sci. Pollut. Res., 30, 85139-85153, 10.1007/s11356-023-28431-x, 2023.
615 Fan, X., Yu, X., Wang, Y., Xiao, X., Li, F., Xie, Y., Wei, S., Song, J., and Peng, P. a.:
616 The aging behaviors of chromophoric biomass burning brown carbon during dark
617 aqueous hydroxyl radical oxidation processes in laboratory studies, Atmos.
618 Environ., 205, 9-18, 10.1016/j.atmosenv.2019.02.039, 2019.
619 Fan, X., Xie, S., Yu, X., Cheng, A., Chen, D., Ji, W., Liu, X., Song, J., Peng, P.
620 Molecular-level transformations of biomass burning-derived water-soluble
621 organic carbon during dark aqueous OH oxidation: Insights from absorption,
622 fluorescence, high-performance size exclusion chromatography and high-
623 resolution mass spectrometry analysis. Sci. Total. Environ., 912, 169290,
624 https://doi.org/10.1016/j.scitotenv.2023.169290, 2024.
625 Fan, X., Cai, F., Xu, C., Yu, X., Wang, Y., Xiao, X., Ji, W., Cao, T., Song, J., Peng, P.
626 Molecular weight-dependent abundance, absorption, and fluorescence
627 characteristics of water-soluble organic matter in atmospheric aerosols. Atmos.
628 Environ., 247, 118159, https://doi.org/10.1016/j.atmosenv.2020.118159, 2021.
629 Gallo, F., Uin, J., Sanchez, K. J., Moore, R. H., Wang, J., Wood, R., Mei, F., Flynn, C.,
630 Springston, S., Azevedo, E. B., Kuang, C. A., Aiken, A. C. Long-range transported
631 continental aerosol in the eastern North Atlantic: three multiday event regimes
632 influence cloud condensation nuclei. Atmos. Chem. Phys., 23, 4221-4246,
633 https://doi.org/10.5194/acp-23-4221-2023, 2023.

Go, B. R., Li, Y. J., Huang, D. D., Chan, C. K. Aqueous-Phase Photoreactions of Mixed Aromatic Carbonyl Photosensitizers Yield More Oxygenated, Oxidized, and less Light-Absorbing Secondary Organic Aerosol (SOA) than Single Systems. Environ. Sci. Technol., 58, 7924-7936, https://doi.org/10.1021/acs.est.3c10199, 2024.

Gu, X., Chen, B., Liu, H., Feng, Y., Wang, B., He, S., Feng, M., Pan, G., Han, S. Photochemical behavior of dissolved organic matter derived from Alternanthera philoxeroides hydrochar: Insights from molecular transformation and photochemically reactive intermediates. J. Hazard. Mater., 461, 132591, https://doi.org/10.1016/j.jhazmat.2023.132591, 2024.

He, T., Wu, Y., Wang, D., Cai, J., Song, J., Yu, Z., Zeng, X., Peng, P. Molecular compositions and optical properties of water-soluble brown carbon during the autumn and winter in Guangzhou, China. Atmos. Environ., 296, 119573, https://doi.org/10.1016/j.atmosenv.2022.119573, 2023.

He, W., Hur, J. Conservative behavior of fluorescence EEM-PARAFAC components in resin fractionation processes and its applicability for characterizing dissolved organic matter. Water. Res., 83, 217-226, https://doi.org/10.1016/j.watres.2015.06.044, 2015.

Hems, R. F., Schnitzler, E. G., Liu-Kang, C., Cappa, C. D., Abbatt, J. P. D. Aging of Atmospheric Brown Carbon Aerosol. ACS Earth. Space. Chem., 5, 722-748, https://doi.org/10.1021/acsearthspacechem.0c00346, 2021.

Hu, T., Luo, M., Qi, Y., He, D., Chen, L., Xu, Y., Chen, D. Molecular evidence for the production of labile, sulfur-bearing dissolved organic matter in the seep sediments

of the South China Sea. Water. Res., 233, 119732, https://doi.org/10.1016/j.watres.2023.119732, 2023.

Huang, S., Luo, Y., Wang, X., Zhang, T., Lei, Y., Zeng, Y., Sun, J., Che, H., Xu, H., Cao, J., Shen, Z. Optical properties, chemical functional group, and oxidative activity of different polarity levels of water-soluble organic matter in PM2.5 from biomass and coal combustion in rural areas in Northwest China. Atmos. Environ., 283, 119179, https://doi.org/10.1016/j.atmosenv.2022.119179, 2022.

Jiang, H., Cai, J., Feng, X., Chen, Y., Wang, L., Jiang, B., Liao, Y., Li, J., Zhang, G., Mu, Y., Chen, J. Aqueous-Phase Reactions of Anthropogenic Emissions Lead to the High Chemodiversity of Atmospheric Nitrogen-Containing Compounds during the Haze Event. Environ. Sci. Technol., 57, 16500-16511, https://doi.org/10.1021/acs.est.3c06648, 2023.

Laszakovits, J. R., Berg, S. M., Anderson, B. G., O'Brien, J. E., Wammer, K. H., and Sharpless, C. M.: p-Nitroanisole/pyridine and p-nitroacetophenone/pyridine actinometers revisited: quantum yield in comparison to ferrioxalate, Environ. Sci. Technol. Lett., 4, 11-14, 10.1021/acs.estlett.6b00422, 2016.

Lee, H. J., Aiona, P. K., Laskin, A., Laskin, J., Nizkorodov, S. A. Effect of solar radiation on the optical properties and molecular composition of laboratory proxies of atmospheric brown carbon. Environ. Sci. Technol., 48, 10217-10226, https://doi.org/10.1021/es502515r, 2014.

Lee, W. C., Deng, Y., Zhou, R., Itoh, M., Mochida, M., Kuwata, M. Water Solubility Distribution of Organic Matter Accounts for the Discrepancy in Hygroscopicity

among Sub- and Supersaturated Humidity Regimes. Environ. Sci. Technol., 56, 17924-17935, https://doi.org/10.1021/acs.est.2c04647, 2022.

Li, F., Tang, S., Lv, J., He, A., Wang, Y., Liu, S., Cao, H., Zhao, L., Wang, Y., Jiang, G. Molecular-Scale Investigation on the Formation of Brown Carbon Aerosol via Iron-Phenolic Compound Reactions in the Dark. Environ. Sci. Technol., 57, 11173-11184, https://doi.org/10.1021/acs.est.3c04263, 2023.

Li, M., Fan, X., Zhu, M., Zou, C., Song, J., Wei, S., Jia, W., Peng, P. Abundances and light absorption properties of brown carbon emitted from residential coal combustion in China. Environ. Sci. Technol., 53, 595-603, https://doi.org/10.1021/acs.est.8b05630, 2018.

Liu, C., Chen, D., Chen, X. Atmospheric Reactivity of Methoxyphenols: A Review. Environ. Sci. Technol., 56, 2897-2916, https://doi.org/10.1021/acs.est.1c06535, 2022.

Liu, J., Chang, M., Cheng, Z., Zhu, S., Ding, P., Liu, F., Li, J., Zhang, G. High Contribution of South Asian Biomass Burning to Southeastern Tibetan Plateau Air: New Evidence from Radiocarbon Measurement. Environ. Sci. Technol. Lett., 8, 1026-1031, https://doi.org/10.1021/acs.estlett.1c00860, 2021.

Liu, Y., Wang, M., Yin, S., Xie, L., Qu, X., Fu, H., Shi, Q., Zhou, F., Xu, F., Tao, S., and Zhu, D.: Comparing Photoactivities of Dissolved Organic Matter Released from Rice Straw-Pyrolyzed Biochar and Composted Rice Straw, Environ. Sci. Technol., 56, 2803-2815, 10.1021/acs.est.1c08061, 2022.

Malavelle, F. F., Haywood, J. M., Mercado, L. M., Folberth, G. A., Bellouin, N., Sitch,

S., Artaxo, P. Studying the impact of biomass burning aerosol radiative and climate effects on the Amazon rainforest productivity with an Earth system model. Atmos. Chem. Phys., 19, 1301-1326, https://doi.org/10.5194/acp-19-1301-2019, 2019.

Manfrin, A., Nizkorodov, S. A., Malecha, K. T., Getzinger, G. J., McNeill, K., Borduas-Dedekind, N. Reactive Oxygen Species Production from Secondary Organic Aerosols: The Importance of Singlet Oxygen. Environ. Sci. Technol., 53, 8553-8562, https://doi.org/10.1021/acs.est.9b01609, 2019.

Murphy, K. R., Stedmon, C. A., Graeber, D., Bro, R. Fluorescence spectroscopy and multi-way techniques. PARAFAC. Anal. Meth., 5, 6557, https://doi.org/10.1039/c3ay41160e, 2013.

Murphy, K. R., Timko, S. A., Gonsior, M., Powers, L. C., Wunsch, U. J., Stedmon, C. A. Photochemistry Illuminates Ubiquitous Organic Matter Fluorescence Spectra. Environ. Sci. Technol., 52, 11243-11250, https://doi.org/10.1021/acs.est.8b02648, 2018.

Podgorski, D. C., Zito, P., McGuire, J. T., Martinovic-Weigelt, D., Cozzarelli, I. M., Bekins, B. A., Spencer, R. G. M. Examining Natural Attenuation and Acute Toxicity of Petroleum-Derived Dissolved Organic Matter with Optical Spectroscopy. Environ. Sci. Technol., 52, 6157-6166, https://doi.org/10.1021/acs.est.8b00016, 2018.

Pucher, M., Wünsch, U., Weigelhofer, G., Murphy, K., Hein, T., Graeber, D. staRdom: Versatile Software for Analyzing Spectroscopic Data of Dissolved Organic Matter in R. Water., 11, 11, https://doi.org/10.3390/w11112366, 2019.

722 Schnitzler, E. G., Gerrebos, N. G. A., Carter, T. S., Huang, Y., Heald, C. L., Bertram, A.
723 K., Abbatt, J. P. D. Rate of atmospheric brown carbon whitening governed by
724 environmental conditions. P. Natl. Acad. Sci. USA, 119, e2205610119,
725 https://doi.org/10.1073/pnas.2205610119, 2022.
726 Smith, J. D., Kinney, H., Anastasio, C. Phenolic carbonyls undergo rapid aqueous
727 photodegradation to form low-volatility, light-absorbing products. Atmos.
728 Environ., *126*, 36-44, https://doi.org/10.1016/j.atmosenv.2015.11.035, 2016.
729 Song, J., Li, M., Jiang, B., Wei, S., Fan, X., Peng, P. Molecular Characterization of
730 Water-Soluble Humic like Substances in Smoke Particles Emitted from
731 Combustion of Biomass Materials and Coal Using Ultrahigh-Resolution
732 Electrospray Ionization Fourier Transform Ion Cyclotron Resonance Mass
733 Spectrometry. Environ. Sci. Technol., 52, 2575-2585,
734 https://doi.org/10.1021/acs.est.7b06126, 2018.
735 Song, J., Li, M., Zou, C., Cao, T., Fan, X., Jiang, B., Yu, Z., Jia, W., Peng, P. Molecular
736 Characterization of Nitrogen-Containing Compounds in Humic-like Substances
737 Emitted from Biomass Burning and Coal Combustion. Environ. Sci. Technol., 56,
738 119-130, https://doi.org/10.1021/acs.est.1c04451, 2022.
739 Song, J., Li, M., Fan, X., Zou, C., Zhu, M., Jiang, B., Yu, Z., Jia, W., Liao, Y., Peng, P.
740 Molecular Characterization of Water- and Methanol-Soluble Organic Compounds
741 Emitted from Residential Coal Combustion Using Ultrahigh-Resolution
742 Electrospray Ionization Fourier Transform Ion Cyclotron Resonance Mass
743 Spectrometry. Environ. Sci. Technol., 53, 13607-13617,

744 https://doi.org/10.1021/acs.est.9b04331, 2019.
745 Sumlin, B. J., Pandey, A., Walker, M. J., Pattison, R. S., Williams, B. J., Chakrabarty,
746 R. K. Atmospheric Photooxidation Diminishes Light Absorption by Primary
747 Brown Carbon Aerosol from Biomass Burning. Environ. Sci. Technol. Lett., 4,
748 540-545, https://doi.org/10.1021/acs.estlett.7b00393, 2017.
749 Sun, W., Guo, Z., Peng, X., Lin, J., Fu, Y., Yang, Y., Zhang, G., Jiang, B., Liao, Y., Chen,
750 D., Wang, X., Bi, X. Molecular characteristics, sources and transformation of
751 water-insoluble organic matter in cloud water. Environ. Pollut., 325, 121430,
752 https://doi.org/10.1016/j.envpol.2023.121430, 2023.
753 Sun, Y., Zhang, Q., Zheng, M., Ding, X., Edgerton, E. S., Wang, X. Characterization
754 and source apportionment of water-soluble organic matter in atmospheric fine
755 particles ($PM_{2.5}$) with high-resolution aerosol mass spectrometry and GC-MS.
756 Environ. Sci. Technol., 45, 4854-4861, https://doi.org/10.1021/es200162h, 2011.
757 Tang, J., Li, J., Su, T., Han, Y., Mo, Y., Jiang, H., Cui, M., Jiang, B., Chen, Y., Tang, J.,
758 Song, J., Peng, P., Zhang, G. Molecular compositions and optical properties of
759 dissolved brown carbon in biomass burning, coal combustion, and vehicle
760 emission aerosols illuminated by excitation–emission matrix spectroscopy and
761 Fourier transform ion cyclotron resonance mass spectrometry analysis. Atmos.
762 Chem. Phys., 20, 2513-2532, https://doi.org/10.5194/acp-20-2513-2020, 2020.
763 Waggoner, D. C., Chen, H. M., Willoughby, A. S., Hatcher, P. G. Formation of black
764 carbon-like and alicyclic aliphatic compounds by hydroxyl radical initiated
765 degradation of lignin. Organ. Geochem., 82, 69-76,

https://doi.org/10.1016/j.orggeochem.2015.02.007, 2015.

Wang, L., Shen, Z., Lu, D., Zhang, Q., Zhang, T., Lei, Y., Xu, H. Water-soluble components in rainwater over Xi'an in northwest China: Source apportionment and pollution controls effectiveness evaluation. Atmos. Pollut. Res., 10, 395-403, https://doi.org/10.1016/j.apr.2018.08.011, 2019.

Wong, J. P. S., Nenes, A., Weber, R. J. Changes in Light Absorptivity of Molecular Weight Separated Brown Carbon Due to Photolytic Aging. Environ. Sci. Technol., 51, 8414-8421, https://doi.org/10.1021/acs.est.7b01739, 2017.

Wong, J. P. S., Tsagkaraki, M., Tsiodra, I., Mihalopoulos, N., Violaki, K., Kanakidou, M., Sciare, J., Nenes, A., Weber, R. J. Effects of Atmospheric Processing on the Oxidative Potential of Biomass Burning Organic Aerosols. Environ. Sci. Technol., 53, 6747-6756, https://doi.org/10.1021/acs.est.9b01034, 2019.

Yan, W., Chen, Y., Han, L., Sun, K., Song, F., Yang, Y., and Sun, H.: Pyrogenic dissolved organic matter produced at higher temperature is more photoactive: Insight into molecular changes and reactive oxygen species generation, J. Hazard. Mater., 425, 10.1016/j.jhazmat.2021.127817, 2022.

Yang, J., Au, W. C., Law, H., Lam, C. H., Nah, T. Formation and evolution of brown carbon during aqueous-phase nitrate-mediated photooxidation of guaiacol and 5-nitroguaiacol. Atmos. Environ., 254, 118401, https://doi.org/10.1016/j.atmosenv.2021.118401, 2021.

Ye, Z., Hu, D., Wang, Z., Wang, H., Ge, X. Aqueous photochemical aging of water-soluble smoke particles from crop straws burning. Atmos. Environ., 340, 120879,

https://doi.org/10.1016/j.atmosenv.2024.120897, 2025.

Ye, Z., Zhuang, Y., Chen, Y., Zhao, Z., Ma, S., Huang, H., Chen, Y., Ge, X. Aqueous-phase oxidation of three phenolic compounds by hydroxyl radical: Insight into secondary organic aerosol formation yields, mechanisms, products and optical properties. Atmos. Environ., 223,117240, https://doi.org/10.1016/j.atmosenv.2019.117240, 2020.

Zhang, B., Shen, Z., He, K., Sun, J., Huang, S., Xu, H., Li, J., Ho, S. S. H., Cao, J. Insight into the Primary and Secondary Particle-Bound Methoxyphenols and Nitroaromatic Compound Emissions from Solid Fuel Combustion and the Updated Source Tracers. Environ. Sci. Technol., 57, 14280-14288, https://doi.org/10.1021/acs.est.3c04370, 2023.

Zhang, R., Gen, M., Liang, Z., Li, Y. J., Chan, C. K. Photochemical Reactions of Glyoxal during Particulate Ammonium Nitrate Photolysis: Brown Carbon Formation, Enhanced Glyoxal Decay, and Organic Phase Formation. Environ. Sci. Technol., 56, 1605-1614, https://doi.org/10.1021/acs.est.1c07211, 2022.

Zhao, R., Lee, A. K. Y., Huang, L., Li, X., Yang, F., Abbatt, J. P. D. Photochemical processing of aqueous atmospheric brown carbon. Atmos. Chem. Phys., 15, 6087-6100, https://doi.org/10.5194/acp-15-6087-2015, 2015.

Zhao, R., Zhang, Q., Xu, X., Wang, W., Zhao, W., Zhang, W., Zhang, Y. Effect of photooxidation on size distribution, light absorption, and molecular compositions of smoke particles from rice straw combustion. Environ. Pollut., 311, 119950, https://doi.org/10.1016/j.envpol.2022.119950, 2022.

Zheng, J., Hu, M., Du, Z., Shang, D., Gong, Z., Qin, Y., Fang, J., Gu, F., Li, M., Peng, J., Li, J., Zhang, Y., Huang, X., He, L., Wu, Y., Guo, S. Influence of biomass burning from South Asia at a high-altitude mountain receptor site in China. Atmos. Chem. Phys., 17, 6853-6864, https://doi.org/10.5194/acp-17-6853-2017, 2017.

Zou, C., Cao, T., Li, M., Song, J., Jiang, B., Jia, W., Li, J., Ding, X., Yu, Z., Zhang, G., Peng, P. Measurement report: Changes in light absorption and molecular composition of water-soluble humic-like substances during a winter haze bloom-decay process in Guangzhou, China. Atmos. Chem. Phys., 23, 963-979, https://doi.org/10.5194/acp-23-963-2023, 2023.

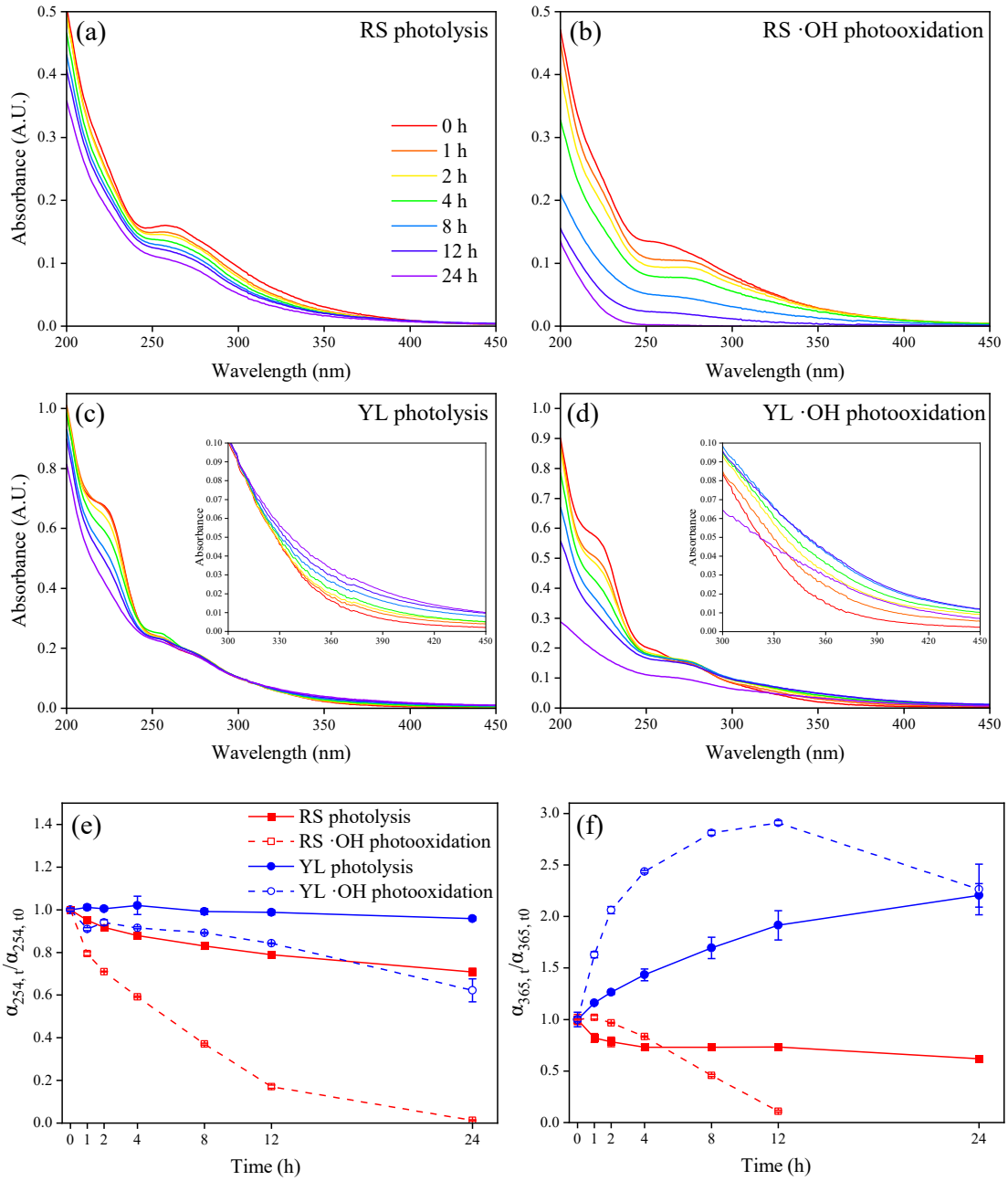

Figure 1. UV-vis spectra of RS and YL WSOM during photolysis (a and c) and ·OH photooxidation (b and d) (The insert figure in c and d represent UV-vis spectra in wavelength range 300-450 nm of YL WSOM during photolysis and ·OH photooxidation), and changes in α_{254} (e) and α_{365} (f) of RS and YL WSOM during photolysis and ·OH photooxidation. The error bars represent one standard deviation (±1σ) of the triplicate samples.

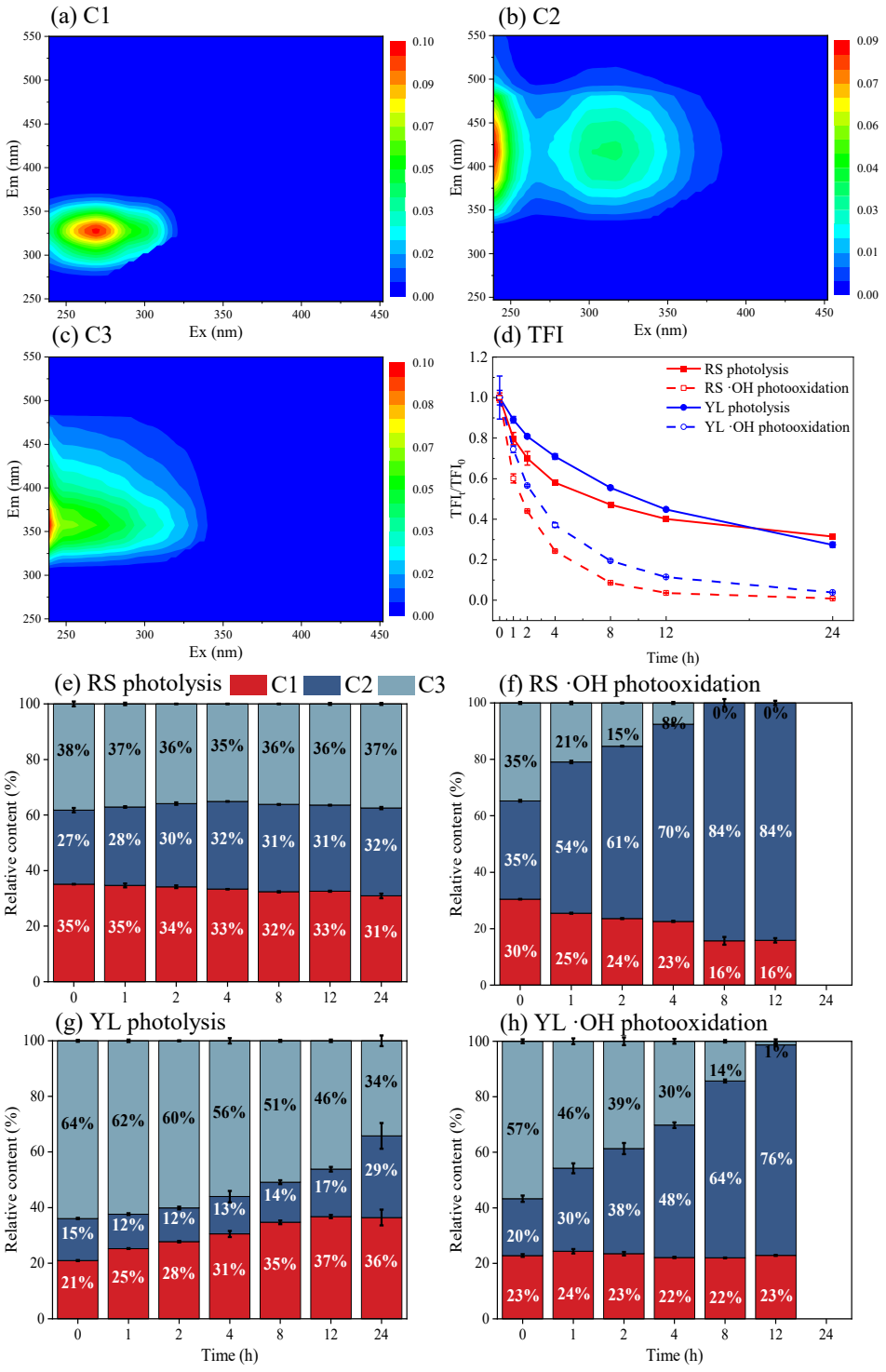

Figure 2. (a-c) EEM spectra of PARAFAC-derived fluorescence components (C1–C3) in RS and YL WSOM. Changes of total fluorescence intensity (TFI) (d) and the relative content of three individual fluorescence component within RS and YL WSOM during photolysis and ·OH photooxidation (e, f, g, h). The error bars represent one standard deviation (±1σ) of the triplicate samples.

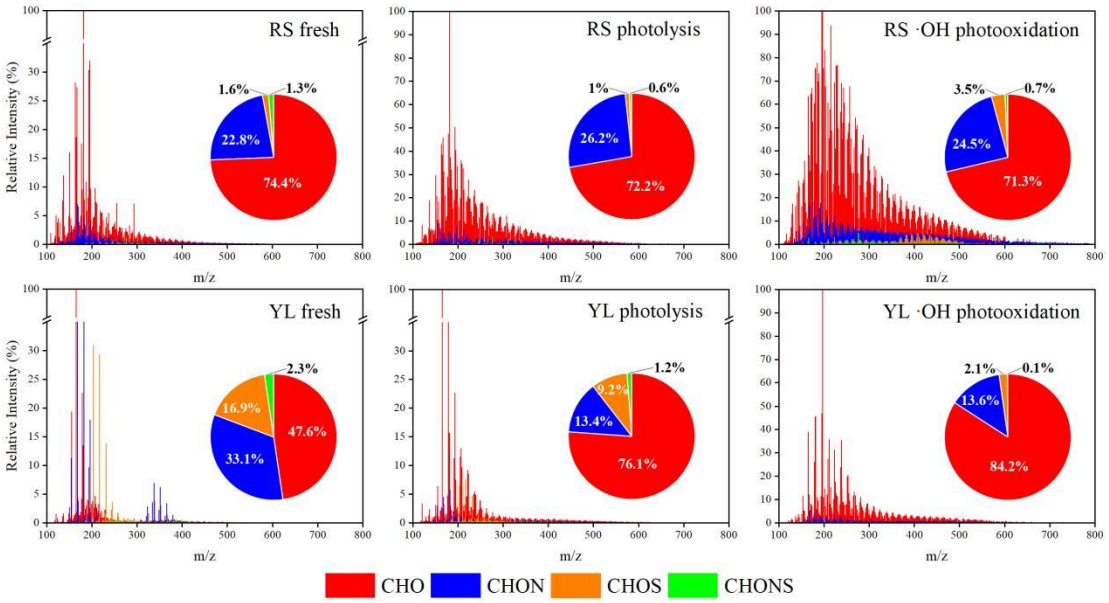

837

838 **Figure 3.** Reconstructed mass spectra of RS and YL WSOM for fresh (left), photolysis (middle)

839 and ·OH photooxidation (right). Pie charts inserted represent the relative content of different

840 formula groups in each sample by sum of intensities of all identified peaks.

841

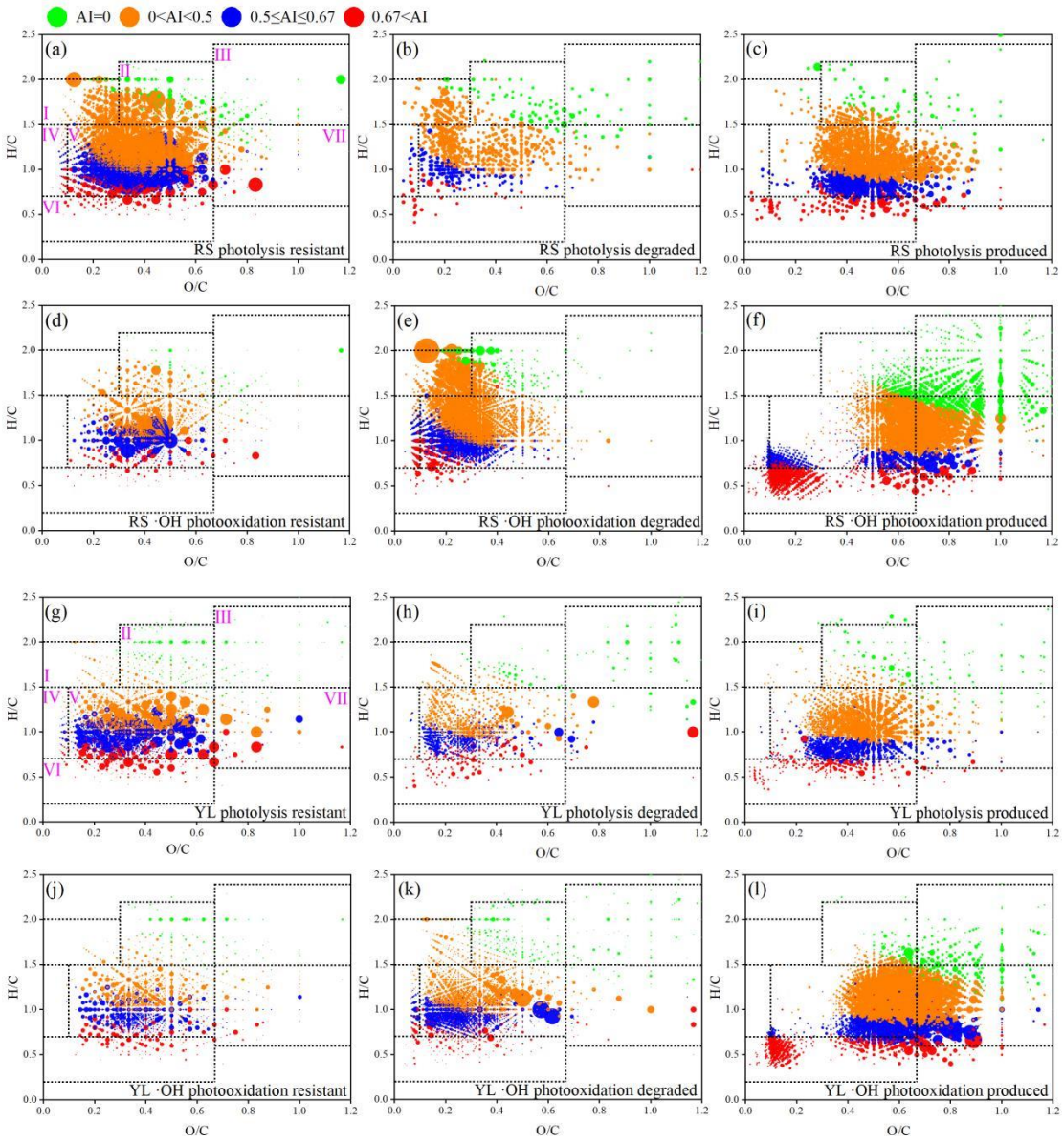

Figure 4. Van Krevelen diagrams for molecules resistant, degraded and produced after photolysis and ·OH photooxidation for RS WSOM (upper) and YL WSOM (bottom).